



1 **Global estimates of reactive nitrogen components during 2000-2100**
2 **based on the multi-stage model**

3 Rui Li^{a, b*}, Yining Gao^a, Lijia Zhang^a, Yubing Shen^a, Gehui Wang^a

4 ^a *Key Laboratory of Geographic Information Science of the Ministry of Education, School of*
5 *Geographic Sciences, East China Normal University, Shanghai, 200241, PR China*

6 ^b *Institute of Eco-Chongming (IEC), 20 Cuinia Road, Chenjia Town, Chongming District,*
7 *Shanghai, 202162, China*

8 * **Corresponding author**

9 Prof. Li (rli@geo.ecnu.edu.cn)

10 **Abstract**

11 High contents of reactive nitrogen components aggravate air pollution and could also impact
12 ecosystem structure and function across the terrestrial-aquatic-marine continuum. However, the
13 long-term historical trends and future prediction of reactive nitrogen components at the global scale
14 still remains high uncertainties. In our study, the field observations, satellite products, model output,
15 and many other covariates were integrated into the machine-learning model to capture the global
16 patterns of reactive nitrogen components during 2000-2019. In order to decrease the estimate
17 uncertainties in the future scenarios, the constructed reactive nitrogen component dataset during the
18 historical period was then utilized as the constraint to calibrate the CMIP6 dataset in four scenarios.
19 The results suggested the cross-validation (CV) R^2 values of four species showed satisfied
20 performance ($R^2 > 0.55$). The concentrations of estimated reactive nitrogen components in China
21 experienced persistent increases during 2000-2013, while they suffered from drastic decreases since
22 2013 except NH_3 . It might be associated with the impact of clean air policy. However, these
23 compounds in Europe and the United States remained relatively stable since 2000. In the future
24 scenarios, SSP3-7.0 (traditional energy scenario) and SSP1-2.6 (carbon neutrality scenario) showed
25 the highest and lowest reactive nitrogen component concentrations, respectively. Although the
26 reactive nitrogen concentrations in some heavy-pollution scenarios (SSP3-7.0) also experienced
27 decreases during 2020-2100, SSP1-2.6 and SSP2-4.5 (middle emission scenario) still kept more
28 rapid decreasing trends. Our results emphasize the need for carbon-neutrality pathway to reduce
29 global atmospheric N pollution.



30 **1. Introduction**

31 Along with the development of global urbanization and industrialization, the anthropogenic
32 emissions of reactive nitrogen (e.g., NO_x, NH₃, HNO₃) experienced drastic increases during the past
33 decades (Chen et al., 2021; Liu et al., 2020b; McDuffie et al., 2020). The reactive nitrogen released
34 from anthropogenic source could significantly alter the global nitrogen cycle throughout the Earth
35 system (Altieri et al., 2021; Zhang et al., 2020). Reactive nitrogen in the atmosphere dominates the
36 chemical formation of tropospheric O₃ and aggravates the particle pollution (Geddes and Martin,
37 2017), with implications for global air quality and climate change (He et al., 2022; Von
38 Schneidemesser et al., 2015). Moreover, the ambient reactive nitrogen could be deposited into the
39 land surface and could cause lake eutrophication and soil acidification (Bouwman et al., 2002; Chen
40 et al., 2018). Therefore, it is highly necessary to understand the spatial distributions and temporal
41 evolution trends of reactive nitrogen components at the global scale.

42 Despite the global importance, observational constraints on reactive nitrogen in the atmosphere
43 were still scarce in most parts of the world (Liu et al., 2020b). Furthermore, the majority of
44 monitoring sites focused on China, Europe, and the United States (Du et al., 2014; Li et al., 2020;
45 Li et al., 2019a; Li et al., 2016), and these uneven sites only possessed limited spatial
46 representativeness (Shi et al., 2018), which restricted the accurate assessment of global reactive
47 nitrogen pollution. Fortunately, the satellite observations gave us a unprecedented chance to capture
48 the global variations of atmospheric reactive nitrogen. Geddes et al. (2017) used the satellite
49 products to calibrate the simulated reactive nitrogen oxides (NO_y) and improved the predictive
50 performance ($R = 0.83$) compared with the chemical transport model (CTM) output alone (Geddes
51 and Martin, 2017). Afterwards, Liu et al. (2022) also used the similar method to estimate the global
52 wet deposition of reduced nitrogen (NH₄⁺) and the R value achieved 0.80 (Liu et al., 2021). Although
53 the calibration based on satellite products could improve the predictive accuracy compared with
54 CTM output, the simulated values still largely biased from the ground-level observations. Moreover,
55 the method cannot accurately fill the gaps of reactive nitrogen concentrations without satellite
56 coverage. In our previous works, we developed a satellite-based ensemble machine-learning model
57 to predict the wet NH₄⁺ deposition across China and the R² value reached 0.76 ($R = 0.88$) (Li et al.,
58 2020). However, this technique was not expanded to the global scale and the high-accuracy and full-



59 coverage global ambient reactive nitrogen dataset was still lack.

60 Apart from the historical estimates, the future prediction of reactive nitrogen is also important
61 because these components in the future scenarios could significantly affect the land carbon cycle
62 and greenhouse gas emissions (Chen et al., 2015; Zaehe, 2013). To the best of our knowledge, only
63 two studies focused on global aerosol prediction in the future scenarios. Chen et al. (2023) predicted
64 the global PM_{2.5} levels and associated mortalities in 2100 under different climate scenarios and
65 found that SSP3-7.0 scenario was linked with the highest PM_{2.5} exposure. Li et al., (2022) also
66 simulated the global NO₃⁻ and NH₄⁺ levels in the future four scenarios and demonstrated that both
67 of these components showed marked decreases in most cases except SSP5-8.5 scenario. However,
68 this study predicted the future reactive nitrogen based on historical CTM output alone, which lacks
69 of observation constraints. The result might increase the uncertainty of assessment.

70 In our study, we developed a multi-stage model to estimate the concentrations of four reactive
71 nitrogen species (NO₃⁻, HNO₃, NH₃, and NH₄⁺) during 2000-2019 because these species were most
72 important reactive nitrogen components for human health and ecological ecosystem and also
73 showed abundant ground-level observations. Then, the species over the 2020-2100 period under the
74 SSP1-2.6, SSP2-4.5, SSP3-7.0, and SSP5-8.5 scenarios were also corrected based on the historical
75 estimates. Finally, the long-term dataset of reactive nitrogen during 2000-2100 was constructed. Our
76 results were beneficial to assess the impacts of reactive nitrogen components on air pollution and
77 climate change in the future.

78 **2. Material and methods**

79 **2.1 Reactive nitrogen observations**

80 Most of reactive nitrogen observations focused on East Asia, Europe, and the United States. The
81 monthly reactive nitrogen components monitoring data during 2010-2015 in China were
82 downloaded from nationwide nitrogen deposition monitoring network (NNDMN) including 32 sites,
83 and these sites could be classified into three types mixed with urban, rural, and background sites
84 (Xu et al., 2019) (Table S1). The concentrations of reactive nitrogen components were determined
85 using the active DENuder for Long-Term Atmospheric sampling system (DELTA). The detailed
86 sampling and analysis procedures have been described by Xu et al. (2019). The dataset of reactive
87 nitrogen components in other countries of East Asia during 2000-2019 were download from the



88 Acid Deposition Monitoring Network in East Asia (EANET). The European Monitoring and
89 Evaluation Programme (EMEP) provides records of long-term reactive nitrogen components in 86
90 sites of most countries across West Europe. Monthly reactive nitrogen components dataset in 84
91 locations across the United States could be obtained from the Clean Air Status and Trends Network
92 (CASTNET) (Figure S1).

93 2.2 Data preparation

94 The GEOS-Chem (v13.4.0) model driven by MERRA2 meteorological parameters was applied
95 to simulate the historical reactive nitrogen components (daily) during 2000-2019 (Feng et al., 2021).
96 The GEOS-Chem model was composed of detailed ozone-NO_x-VOC-PM-halogen tropospheric
97 chemistry. The grid version of the model with a horizontal resolution of 2° × 2.5° was utilized. Wet
98 deposition contained many processes including sub-grid scavenging in convective updrafts, in-
99 cloud rainout, and below-cloud washout (Liu et al., 2001). Dry deposition was estimated based on
100 a resistance-in-series model (Wesely, 2007). The anthropogenic emission inventory in 2000-2019
101 was downloaded from the website of Community Emissions Data System (CEDS) (Hoesly et al.,
102 2018). Then, the daily reactive nitrogen components were averaged to the monthly scale.

103 The IASI instrument aboard on the polar sun-synchronous MetOp platform traverses the
104 equator twice each day (9:30 a.m. and 9:30 p.m. local solar time) (Whitburn et al., 2016a). The
105 measurements in the daytime usually shows the better accuracy than those at night due to the high
106 sensitivity to ambient NH₃ (Van Damme et al., 2017; Whitburn et al., 2016a; Whitburn et al., 2016b).
107 In our study, we used the IASI NH₃ columns in morning during 2008-2019 to estimate the NH₃ and
108 NH₄⁺ concentrations globally. Besides, the NH₃ column dataset with a cloud shield higher than 25%
109 and relative error above 100% were eliminated.

110 The tropospheric vertical column density (VCD) of NO₂ retrieved from OMI aboard on Aura
111 satellite crosses the earth once a day (Kim et al., 2016). OMI-derived tropospheric NO₂ column
112 densities during 2005-2019 was applied to develop the model. The tropospheric NO₂ column density
113 data with cloud radiance fraction > 0.5, terrain reflectivity > 30%, and solar zenith angles > 85°
114 were screened (Cooper et al., 2022). Additionally, the NO₂ columns from GOME (1995-2003),
115 SCIAMACHY (2002-2011) and GOME-2 (2007-) were also collected to simulate the NO₃⁻ and
116 HNO₃ levels. The similar overpass time of these three instruments (from about 09:30 to 10:30 LT,



117 local time) facilitates the simultaneous use to capture consistent long-term coverage. However, the
118 dataset cannot cover the NO₂ columns since 2017. To overcome the inconsistency of these satellite
119 products, we applied the linear regression technique to construct the relationship between OMI-NO₂
120 columns and GOME/SCIAMACHY NO₂ columns. The results suggested these satellite products
121 showed good relationship ($R^2 > 0.6$). At last, the long-term (2000-2019) NO₂ columns at the global
122 scale were constructed.

123 The monthly meteorological parameters derived from ERA-5 comprise of 2 m dewpoint
124 temperature (D_{2m}), 2 m temperature (T_{2m}), surface pressure (S_p), and total precipitation (T_p), 10 m
125 U wind component (U_{10}), and 10 m V wind component (V_{10}). The population density data during
126 2000-2020 around the world were downloaded from
127 <https://hub.worldpop.org/geodata/listing?id=64>. The elevation data was extracted from ETOPO at a
128 spatial resolution of 1' (Amante and Eakins, 2009) (<https://rda.ucar.edu/datasets/ds759.4/>). In
129 addition, the land use data including cropland, forest, grassland, shrubland, tundra, barren land, and
130 snow/ice were obtained from Liu et al. (2020a). Besides, the CMIP6 dataset in four scenarios were
131 also applied to predict the reactive nitrogen concentrations during 2020-2100. The dataset includes
132 2-m air temperatures, wind speed at 850 and 500 hPa, total cloud cover, precipitation, relative
133 humidity, and short-wave radiation. The modelled meteorological parameters derived from 16 earth
134 system models were incorporated into the machine-learning model. The detailed models are
135 summarized in Table S2.

136 2.3 Model development

137 A three-stage model was established to capture the full-coverage reactive nitrogen dataset at
138 the global scale (Figure 1). In the first stage, the ground-level reactive nitrogen species, satellite
139 products (e.g., OMI-NO₂ and IASI-NH₃ columns), meteorological factors, land use types,
140 population, and simulated reactive nitrogen components derived from GEOS-Chem model were
141 collected as the independent variables to estimate the gridded reactive nitrogen species at the
142 period/grid with satellite product based on LightGBM algorithm. In the second stage, the
143 meteorological parameters, GEOS-Chem output, land use data, and population were applied to fill
144 the gaps without satellite retrievals. Then, the simulated results based on these models were fused
145 to obtain the full-coverage reactive nitrogen components and the ground-level observations were



146 further used to calibrate the full-coverage dataset and the final reactive nitrogen components at the
 147 global scale were simulated. In the last stage, the reactive nitrogen components and meteorological
 148 parameters in four scenarios (SSP1-2.6, SSP2-4.5, SSP3-7.0, and SSP5-8.5) during 2020-2100 were
 149 collected from CMIP6 dataset including 16 earth system models (Table S2). Then, the data in the
 150 future scenarios were integrated into the ensemble model including XGBoost, LightGBM, and
 151 convolutional neural networks (CNN) to further calibrate the modeling results based on historical
 152 dataset (2000-2019) derived from previous two-stage model. The detailed equations of multiple
 153 machine-learning models are summarized as follows:

154 (1) XGBoost model

$$155 \quad F^{(t)} = \sum_{i=1}^n [l(y_i, y^{\Lambda(t-1)}) + \partial_{y^{\Lambda(t-1)}} l(y_i, y^{\Lambda(t-1)}) f_t(x_i) + \frac{1}{2} \partial_{y^{\Lambda(t-1)}}^2 l(y_i, y^{\Lambda(t-1)}) f_t^2(x_i)] + \Omega(f_t) \quad (1)$$

156 where $F^{(t)}$ is the cost function at the t -th period; ∂ is the derivative of the function; $\partial_{y^{\Lambda(t-1)}}^2$
 157 represents the second derivative of the function; l denotes the differentiable convex loss function
 158 that reveals the difference of the predicted value (y^{Λ}) of the i -th instance at the t -th period and the
 159 target value (y_i); $f(x)$ represents the increment; $\Omega(f_t)$ reflects the regularizer.

160 (2) LightGBM model

$$161 \quad \hat{f} = \arg \min_f E_{y,x} Q(y, f(x)) \quad (2)$$

$$162 \quad f_T(X) = \sum_{t=1}^T f_t(X) \quad (3)$$

163 where $Q(y, f(x))$ reflects the a specific loss function; $\sum_{t=1}^T f_t(X)$ denotes the regression trees.

164 (3) CNN model

165 The reactive nitrogen species and meteorological parameters in the future scenarios were applied to
 166 CNN model based on the historical (2000-2019) reactive nitrogen species derived from stage 1-2
 167 model.

$$168 \quad x \xrightarrow{f:U-Net} y \quad (4)$$

169 where x (x_1, x_2, \dots, x_n) represents the reactive nitrogen species and meteorological parameters



170 derived from CMIP6 dataset; y (y_1, y_2, \dots, y_n) denotes the historical (2000-2019) reactive nitrogen
171 species.

172 All of the convolution layers showed the same kernel size of 3×3 and used rectified linear unit
173 (ReLU) as the activation function. Max-pooling layers were employed for adjusting the size of
174 images to capture better bottleneck information. After each block, the image size could be halved
175 by using the max pooling layer with kernel size of 2×2 , but the number of channels will be doubled.
176 In our study, the learning rate was set as 0.1 to achieve the best performance.

177 All of the independent variables collected from multiple sources were resampled to 0.25° grids
178 using appropriate algorithms. For example, both of the population density and land use type in each
179 grid were calculated using spatial clipping toolbox. Later on, all of these variables were combined
180 to develop the model. During the development of multi-stage model, it was highly imperative to
181 remove some redundant explanatory variables and then determine the optimal variable group. The
182 redundant variables means that the overall predictive accuracy could degrade after the removal of
183 these variables.

184 **3. Results and discussion**

185 **3.1 The modelling performance of historical reactive nitrogen estimates**

186 The multi-stage model was applied to capture the spatiotemporal variations of reactive nitrogen
187 concentrations during 2000-2100. In our study, we employed XGBoost model to construct the full-
188 coverage reactive nitrogen dataset during 2000-2020. The cross-validation (CV) R^2 values of the
189 model for NO_3^- , HNO_3 , NH_3 , and NH_4^+ estimates reached 0.67, 0.62, 0.58, and 0.60, respectively
190 (Figure 2). RMSE of NO_3^- , HNO_3 , NH_3 , and NH_4^+ were 0.55, 0.23, 2.32, and $1.71 \mu\text{g N m}^{-3}$,
191 respectively. MAE of NO_3^- , HNO_3 , NH_3 , and NH_4^+ reached 0.19, 0.13, 1.23, and $0.59 \mu\text{g N m}^{-3}$. The
192 CV R^2 values of NO_3^- , HNO_3 , and NH_4^+ estimates were significantly higher than Jia et al. (2016)
193 (0.22, 0.41, and 0.49), while the CV R^2 value of NO_3^- estimate in our study was comparable to
194 Geddes et al. (2017) (0.68) (Geddes and Martin, 2017). The CV R^2 value of NH_3 estimates were
195 also close to the results obtained by Liu et al. (2019) (0.45-0.71) (Liu et al., 2019). Overall, the
196 predictive performances historical reactive nitrogen was satisfied. Although the CV R^2 values in our
197 study were not significantly higher than those in some previous studies, our study developed the
198 full-coverage (gap-free) ambient reactive nitrogen dataset, which was superior to some previous



199 studies. Based on the constructed full-coverage reactive nitrogen dataset, we also developed the
200 ensemble model to calibrate the CMIP6 dataset in the future scenarios. The CV R^2 values of the
201 model for NO_3^- , HNO_3 , NH_3 , and NH_4^+ estimates in the future scenarios reached 0.62, 0.67, 0.56,
202 and 0.60, respectively (Figure S2). RMSE of NO_3^- , HNO_3 , NH_3 , and NH_4^+ were 0.58, 0.26, 2.12,
203 and $1.91 \mu\text{g N m}^{-3}$, respectively. MAE of NO_3^- , HNO_3 , NH_3 , and NH_4^+ reached 0.22, 0.22, 1.04, and
204 $0.65 \mu\text{g N m}^{-3}$. Overall, the ensemble model for these species in the future scenarios still showed
205 satisfied performance, and thus the result could be treated to be robust.

206 3.2 The spatial patterns of nitrogen reactive components

207 The global annual mean concentrations of NO_3^- , HNO_3 , NH_3 , and NH_4^+ during 2000-2019
208 ranged from 0.03 to 9.08, 0.03 to 1.73, 0.21 to 13.9, and 0.08 to $17.1 \mu\text{g N m}^{-3}$ with the mean values
209 of 0.43 ± 0.24 (standard deviation over grids), 0.28 ± 0.13 , 1.79 ± 0.85 , and $0.65 \pm 0.36 \mu\text{g N m}^{-3}$
210 (Figure S3), respectively. China, West Europe, and the United States obtained widespread attention
211 due to the developed economy and dense anthropogenic activity.

212 In China, the overall mean ambient NO_3^- , HNO_3 , NH_3 , and NH_4^+ concentrations reached
213 1.05 ± 0.62 , 0.35 ± 0.19 , 4.05 ± 1.84 , and $2.38 \pm 1.26 \mu\text{g N m}^{-3}$, ranging from 0.07-9.08, 0.06-1.73,
214 0.84-11.6, and 0.18-13.1 $\mu\text{g N m}^{-3}$. At the regional scale, the annual mean NO_3^- , HNO_3 , NH_3 , and
215 NH_4^+ concentrations followed the order of North China Plain (NCP) (4.38, 1.12, 7.22, and $7.69 \mu\text{g N m}^{-3}$) > Sichuan Basin (2.40 ± 1.01 , 0.52 ± 0.28 , 4.92 ± 1.71 , and $6.02 \pm 1.82 \mu\text{g N m}^{-3}$) (Figure
216 3). NCP displayed the higher NO_3^- and HNO_3 concentrations owing to dense human activities and
217 strong industry foundation (Qi et al., 2023; Wen et al., 2018), which could emit a large amount of
218 NO_x to the atmosphere. In both of Yangtze River Delta (YRD) and Pearl River Delta (PRD), the
219 combustion of fossil fuels and traffic emissions might be the major source of NO_x emission, which
220 aggravated nitrate events via gas-particle conversion processes (Huang et al., 2017; Li et al., 2017).
221 For Sichuan Basin, the poor topographical or meteorological conditions were major factors
222 responsible for the severe nitrate pollution (Zhang et al., 2019). It was not surprising that high
223 ambient NH_3 concentrations focused on NCP and Sichuan Basin because most of Chinese croplands
224 are distributed on these regions (Karra et al., 2021; Potapov et al., 2022), which was the major source
225 of NH_3 emissions with frequent N fertilizer applications (Ma et al., 2022). Besides, N manure was
226 another major source of NH_3 emissions in China, and the percentage of N manure to NH_3 emissions
227



228 exceeds 50% (Kang et al., 2016). The spatial pattern of NH_4^+ level was in good agreement with the
229 NH_3 concentration because NH_4^+ was often generated from the reaction of NH_3 with SO_2 and NO_2
230 (Ehrnsperger and Klemm, 2021).

231 In Europe, the ambient NO_3^- , HNO_3 , NH_3 , and NH_4^+ concentrations ranged from 0.13 to 2.84,
232 0.06 to 0.92, 0.35 to 7.81, and 0.22 to 3.77 $\mu\text{g N m}^{-3}$, respectively. The annual mean NO_3^- , HNO_3 ,
233 NH_3 , and NH_4^+ levels reached 0.57 ± 0.28 , 0.25 ± 0.11 , 1.58 ± 0.68 , and 0.89 ± 0.42 $\mu\text{g N m}^{-3}$,
234 respectively (Figure 3). High concentrations of reactive nitrogen components focused on the
235 northern part of Italy, central and southern part of Germany, North France, Poland, and the western
236 part of Russia, which was in good agreement with the spatial pattern of NO_x and NH_3 emissions
237 (Luo et al., 2022; Qu et al., 2020). Emissions Database for Global Atmospheric Research (EDGAR)
238 suggested that N fertilization and N manure accounted for 43% and 53% of total NH_3 emissions in
239 western Europe (Liu et al., 2019), respectively. Furthermore, Liu et al. (2019) confirmed that a good
240 relationship between ambient NH_3 level and N fertilization plus N manure ($r = 0.62$) was observed
241 in Europe. Cooper et al. (2017) employed the inversion model to estimate NO_x emission in Europe
242 and also found that high NO_x emission was also mainly distributed on North France, Germany, the
243 northern part of Italy, and Russia, which partly explained the higher concentrations of reactive
244 nitrogen components in these regions.

245 In the United States, the ambient NO_3^- , HNO_3 , NH_3 , and NH_4^+ concentrations reached $0.28 \pm$
246 0.12 , 0.19 ± 0.08 , 2.12 ± 0.66 , and 0.49 ± 0.25 $\mu\text{g N m}^{-3}$, with the range of 0.03-2.35, 0.03-1.31,
247 0.26-9.96, and 0.10-6.09 $\mu\text{g N m}^{-3}$ (Figure 3), respectively. The hotspots of NO_3^- , HNO_3 , and NH_4^+
248 levels focused on the eastern part of the United States, while the higher NH_3 concentration focused
249 on Central Great Plains and some regions in California such as San Joaquin Valley (6.15 $\mu\text{g N m}^{-3}$).
250 Both of bottom-up and top-down NO_x and NH_3 emissions suggested that the spatial distributions of
251 reactive nitrogen components were strongly dependent on the precursor emissions (McDuffie et al.,
252 2020; Qu et al., 2020).

253 Besides, some other regions such as the northern part of India also experienced severe N
254 pollution in the atmosphere. Meanwhile, some countries in South America such Brazil and
255 Argentina also suffered from serious HNO_3 and NH_3 pollution. The higher ambient NH_3
256 concentration focused on the northern part of India might be contributed by two major reasons. First



257 of all, the intensive agricultural activities and high air temperature might be responsible for the
258 higher NH_3 level (Cui, 2023; Wang et al., 2020). Moreover, the relatively low sulfur dioxide (SO_2)
259 and nitrogen oxides (NO_x) emissions coupled with high air temperature restricted the gas-to-particle
260 conversion of NH_3 (Wang et al., 2020). The severe HNO_3 and NH_3 pollution in Brazil and Argentina
261 might be also linked with the dense agricultural activities (Huneus et al., 2017).

262 3.3 The seasonal variations of reactive nitrogen components

263 The ambient NO_3^- , HNO_3 , NH_3 , and NH_4^+ concentrations exhibited significant seasonal
264 variations (Figure S4-8). NO_3^- , HNO_3 , and NH_4^+ displayed the highest and lowest values in winter
265 (December-February) and summer (June-August), respectively. On the one hand, the anthropogenic
266 NO_x emission for domestic heating might be higher in winter compared with other seasons (Lin et
267 al., 2011). On the other hand, the stagnant meteorological conditions limited the pollutant diffusion
268 (Li et al., 2019b; Liu et al., 2020c). Meanwhile, the higher relative humidity in winter facilitated the
269 formation of NH_4NO_3 (Huang et al., 2016; Xu et al., 2012). However, both of ambient NO_3^- and
270 NH_4^+ concentrations showed the lower concentrations in summer, which might be attributable to
271 the decomposition of NH_4NO_3 under the condition of high air temperature. In contrast to the
272 secondary inorganic nitrogen, the ambient NH_3 level showed the highest concentration in summer
273 ($1.71 \pm 0.45 \mu\text{g N m}^{-3}$). China, Europe, and the United States suffered from similar NH_3 peaks in
274 summer (4.20 ± 1.85 , 1.77 ± 0.65 , and $2.21 \pm 1.04 \mu\text{g N m}^{-3}$). There are two reasons accounting for
275 the fact. At first, mineral N fertilizer or manure application was mainly performed in spring and
276 early summer (Paulot et al., 2014). Many field observations have obtained similar NH_3 peak in
277 summer (He et al., 2021; Pan et al., 2018). Moreover, summer often showed the higher air
278 temperature, which promotes the volatilization of ammonium and limits the gas-to-particle of
279 gaseous NH_3 (Liu et al., 2019).

280 3.4 The historical trends of reactive nitrogen components during 2000-2019

281 The long-term trends of ambient NO_3^- , HNO_3 , NH_3 , and NH_4^+ concentrations are shown in
282 Figure 4 and Figure S9-12. The NO_3^- concentration in China displayed rapid increase (9.7%/yr)
283 during 2000-2007, and then it kept the moderate increase (4.2%/yr) during 2007-2013. However,
284 the NO_3^- concentration in China experienced the drastic decrease (-2.6%/yr) since 2013. The
285 ambient HNO_3 and NH_4^+ concentrations showed similar trends during this period. Due to the impact



286 of Clean Air Action, the concentrations of gaseous precursors (e.g., SO₂ and NO_x) suffered from
287 substantial decreases, which could be transformed into nitrate and ammonium via heterogeneous
288 reactions (Huang et al., 2019). However, the decreasing rates of NO₃⁻ were still much lower than
289 those of gaseous precursors (Li et al., 2023). On the one hand, it might be associated with the
290 increased O₃ level and enhanced atmospheric oxidation capacity (AOC), which led to an increase
291 in the photochemical reaction rate of the secondary components (Wang et al., 2019). On the other
292 hand, strong SO₂ emission control under the Clean Air Action allowed more gaseous NH₃ to form
293 nitrate. The ambient NH₃ level remained relatively stable status during 2000-2013, while it
294 experienced rapid increases after 2013. The result was in good agreement with Liu et al. (2019). In
295 fact, the ambient NH₃ level in North China Plain still experienced dramatic increase (> 0.2 μg N m⁻³
296 /yr) during 2000-2013 because enhanced agricultural activities. Zhang et al. (2017) have
297 demonstrated that the livestock manure and fertilizer application generally accounted for 43.1% and
298 36.4% of the agricultural NH₃ emission, respectively. Since 2013, the NH₃ concentration in the
299 entire China suffered from rapid increase, which might be associated with the drastic decrease of
300 sulfate. It was well known that NH₃ could react with HNO₃ and gaseous H₂SO₄ to generate ammonia
301 sulfate and ammonia nitrate (Wang et al., 2022; Wang et al., 2019). Substantial decreases of acidic
302 gases (e.g., SO₂) lead to the reduction of NH₃ conversion to ammonia salts in the atmosphere (Chen
303 et al., 2019), which result in excess NH₃ remaining in the gaseous phase.

304 Compared with China, the long-term trends of reactive nitrogen components Europe and the
305 United States were relatively stable. In the Europe, the concentrations of NO₃⁻, HNO₃, and NH₃
306 exhibited increases during 2000-2007 (0.7%/yr, 2.3%/yr, and 2.1%/yr), while they experienced
307 slight decreases after 2007. The NH₄⁺ level displayed continuous decrease since 2000. The result
308 was closely linked with the trends of NO_x and NH₃ emissions derived from satellite retrieval
309 (Cooper et al., 2017; Luo et al., 2022). In the United States, both of NO₃⁻ and NH₄⁺ showed persistent
310 decreases during 2000-2019. Zhang et al. (2018) have confirmed that NO_x emission in the eastern
311 US has experienced persistent decrease since 1990, which facilitated the decreases of NO₃⁻ and
312 NH₄⁺ levels. However, the ambient HNO₃ and NH₃ concentrations displayed slight increases during
313 2000-2007 (2.1%/yr), and then remained relatively stable since 2007. Liu et al. (2019) also found
314 similar characteristic of ambient NH₃ trend in the United States. In fact, the NH₃ concentrations in



315 the Middle Plain and eastern US still showed increases due to the lack of NH₃ emission control
316 policies as well as the decline in acidic gases (Warner et al., 2017).

317 3.5 Projection of future ambient reactive nitrogen components

318 For the future reactive nitrogen component estimates, the ensemble model was applied to
319 predict the reactive nitrogen component concentrations under the SSP1-2.6, SSP2-4.5, SSP3-7.0,
320 and SSP5-8.5 scenarios. The whole period (2021-2100) could be uniformly classified into four
321 periods including 2021-2040 (2030s), 2041-2060 (2050s), 2061-2080 (2070s), and 2081-2100
322 (2090s), respectively. In SSP1-2.6, the projected global mean NO₃⁻ concentrations decreased from
323 $0.40 \pm 0.12 \mu\text{g N m}^{-3}$ during 2030s to $0.38 \pm 0.11 \mu\text{g N m}^{-3}$ during 2090s (Figure 5a-d and Figure
324 S13). SSP2-4.5 scenario represents the middle range of plausible future pathways (Nazarenko et al.,
325 2022), and the predicted global average NO₃⁻ concentrations in this scenario decreased from $0.40 \pm$
326 $0.14 \mu\text{g N m}^{-3}$ during 2030s to $0.37 \pm 0.12 \mu\text{g N m}^{-3}$ during 2090s. SSP3-7.0 and SSP5-8.5 denote
327 the less investment in the environment and heavily relies on traditional energy for rapid economic
328 development, respectively. The ambient NO₃⁻ levels in these scenarios showed more remarkable
329 decreases from 2030s to 2090s. For instance, the NO₃⁻ concentrations in China decreased from 1.07
330 ± 0.36 and $1.01 \pm 0.30 \mu\text{g N m}^{-3}$ to 0.84 ± 0.46 and $0.60 \pm 0.34 \mu\text{g N m}^{-3}$, respectively. The NO₃⁻
331 levels in India also experienced rapid increases from 2.21 ± 1.04 to $3.30 \pm 1.58 \mu\text{g N m}^{-3}$ in SSP3-
332 7.0 scenario, while they suffered from marked decreases from 2.33 ± 1.12 to $1.60 \pm 0.84 \mu\text{g N m}^{-3}$
333 in SSP5-8.5 scenario.

334 The projected global average HNO₃ concentrations remained relatively stable from 0.26 ± 0.13
335 and $0.27 \pm 0.14 \mu\text{g N m}^{-3}$ during 2030s to 0.25 ± 0.12 and $0.26 \pm 0.13 \mu\text{g N m}^{-3}$ during 2090s in
336 SSP1-2.6 and SSP2-4.5 scenarios, respectively (Figure 6a-d and Figure S14). However, some
337 developing countries such as China and India experienced drastic HNO₃ changes during these
338 scenarios. The mean HNO₃ concentrations in China and India decreased from 0.29 ± 0.17 and 0.43
339 $\pm 0.25 \mu\text{g N m}^{-3}$ to 0.26 ± 0.15 and $0.35 \pm 0.22 \mu\text{g N m}^{-3}$ in SSP1-2.6 scenario, respectively. In SSP2-
340 4.5 scenario, the average HNO₃ concentrations in China and India decreased from 0.31 ± 0.20 and
341 $0.55 \pm 0.29 \mu\text{g N m}^{-3}$ in 2030s to 0.27 ± 0.18 and $0.45 \pm 0.25 \mu\text{g N m}^{-3}$ in 2090s, respectively.
342 Compared with SSP1-2.6 and SSP2-4.5, the heavy-pollution scenarios (e.g., SSP3-7.0 and SSP5-
343 8.5) showed the higher HNO₃ concentrations. The HNO₃ concentrations in China decreased from



344 0.34 ± 0.21 and $0.31 \pm 0.20 \mu\text{g N m}^{-3}$ in 2030s to 0.31 ± 0.20 and $0.28 \pm 0.14 \mu\text{g N m}^{-3}$ in 2090s for
345 SSP3-7.0 and SSP5-8.5 scenarios, respectively. The HNO_3 concentrations in India also experienced
346 rapid increases from 0.54 ± 0.29 to $0.70 \pm 0.38 \mu\text{g N m}^{-3}$ in SSP3-7.0 scenario. It was assumed that
347 the government gave less investment in environment improvement and the anthropogenic emission
348 did not show marked decrease under the condition of SSP3-7.0 scenario. However, the ambient
349 HNO_3 levels suffered from marked decreases from 0.63 ± 0.28 to $0.51 \pm 0.22 \mu\text{g N m}^{-3}$ in SSP5-8.5
350 scenario. Although the SSP5-8.5 scenario is heavily dependent on the fossil fuel production (Chen
351 et al., 2020), the anthropogenic emission still displayed gradual decrease during the 80-year period.

352 The higher ambient NH_3 concentrations also focused on China and India (Figure 7 and Figure
353 S15). In SSP1-2.6, the ambient NH_3 concentrations in China and India decreased from 2.92 and
354 $5.59 \mu\text{g N m}^{-3}$ during 2030s to 1.77 and $2.73 \mu\text{g N m}^{-3}$ during 2090s, respectively. In SSP2-4.5, the
355 ambient mean NH_3 concentrations in China and India decreased from 3.43 and $7.57 \mu\text{g N m}^{-3}$ during
356 2030s to 2.06 and $5.33 \mu\text{g N m}^{-3}$ during 2090s, respectively. Compared with SSP1-2.6 and SSP2-
357 4.5, the ambient NH_3 concentrations in heavy-pollution scenarios did not show marked decreases
358 from 2020-2100, which might be associated with ineffective NH_3 emission control. The temporal
359 variations of ambient NH_4^+ levels in the future scenarios show similar trends with NH_3 . The
360 atmospheric NH_4^+ levels in China decreased from 1.53 (SSP1-2.6), 1.95 (SSP2-4.5), 2.31 (SSP3-
361 7.0), and $1.87 \mu\text{g N m}^{-3}$ (SSP5-8.5) during 2030s to 0.60, 0.84, 1.78, and $0.97 \mu\text{g N m}^{-3}$ during 2090s,
362 respectively (Figure 8 and Figure S16). Meanwhile, the ambient NH_4^+ levels in India changed from
363 3.68 (SSP1-2.6), 5.31 (SSP2-4.5), 5.49 (SSP3-7.0), and $6.07 \mu\text{g N m}^{-3}$ (SSP5-8.5) during 2030s to
364 1.38, 3.49, 6.89, and $2.96 \mu\text{g N m}^{-3}$ during 2090s, respectively.

365 3.6 Implications and limitations

366 Global trends of four reactive nitrogen components during 2000-2100 emphasizes the urgent
367 mitigation measures (carbon neutrality pathway) to reduce precursor emissions in order to decrease
368 the concentrations and depositions of reactive nitrogen components especially in China and India.
369 Furthermore, our result could give valuable insights into the impact of reactive nitrogen components
370 on human health and ecological environment. However, this study still shows some limitations. First
371 of all, the observation networks mainly focus on China, Europe, and the United States, and thus the
372 simulations in many other regions might show large uncertainties. Secondly, the CMIP6 future



373 climate scenario data also exhibits large uncertainties, which could impact the reliability of this
374 study. Lastly, our predictions were performed on the basis of the premise that the world was steadily
375 developing, and cannot predict the impacts of uncontrollable factors (e.g., COVID-19, Russia-
376 Ukraine War).

377 **Competing interests**

378 The contact author has declared that none of the authors has any competing interests.

379 **Acknowledgements**

380 This work was supported by the National Natural Science Foundation of China (U23A2030).

381 **Data availability**

382 The CMIP6 dataset used in this publication is available in [https://esgf.nci.org.au/projects/cmip6-](https://esgf.nci.org.au/projects/cmip6-nci/)
383 [nci/](https://esgf.nci.org.au/projects/cmip6-nci/).

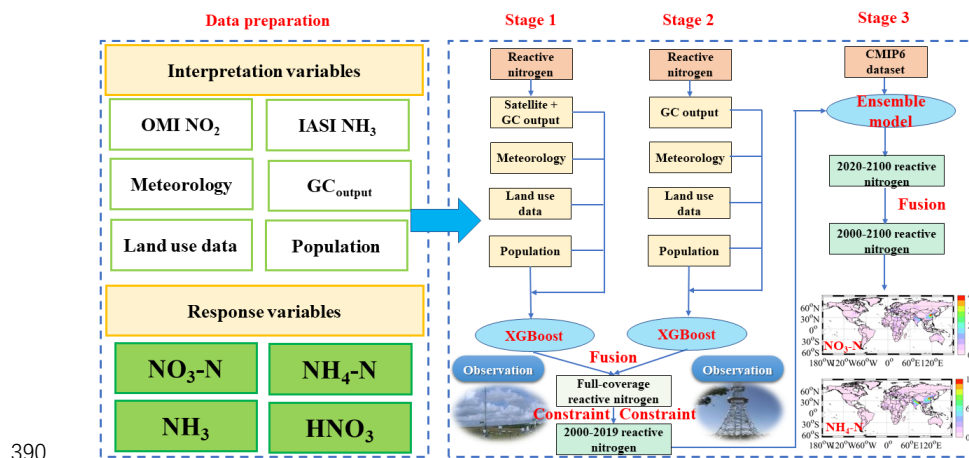
384 **Author contributions**

385 LR and WGH designed the study; LR developed the model; GYN, ZLJ, and SYB analyzed the
386 observation and model data. LR wrote this manuscript.

387

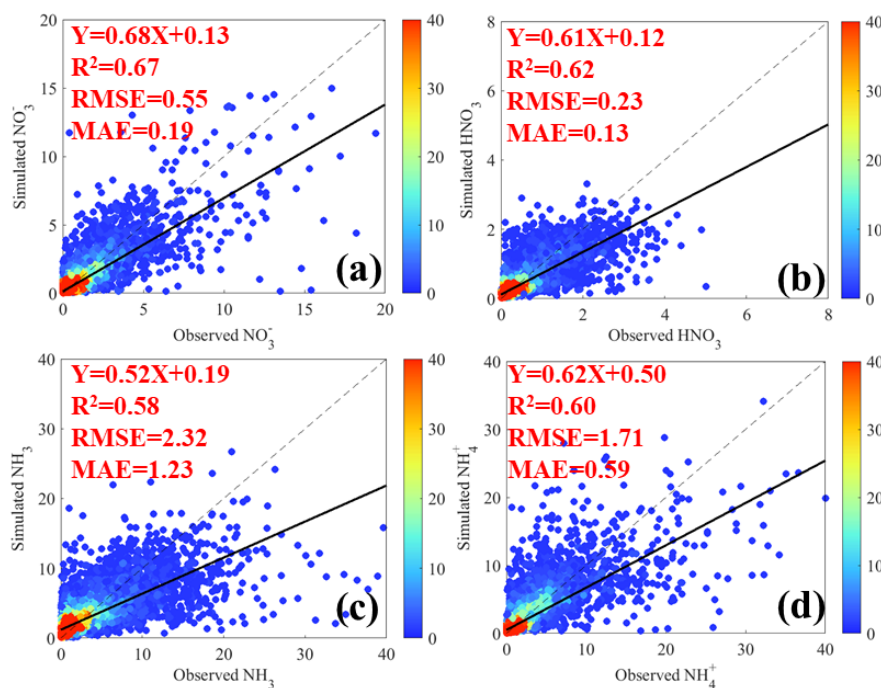


388 **Figure 1** The workflow of global full-coverage reactive nitrogen estimates during 2000-2100.
 389 GC_{output} denotes the GEOS-Chem output.





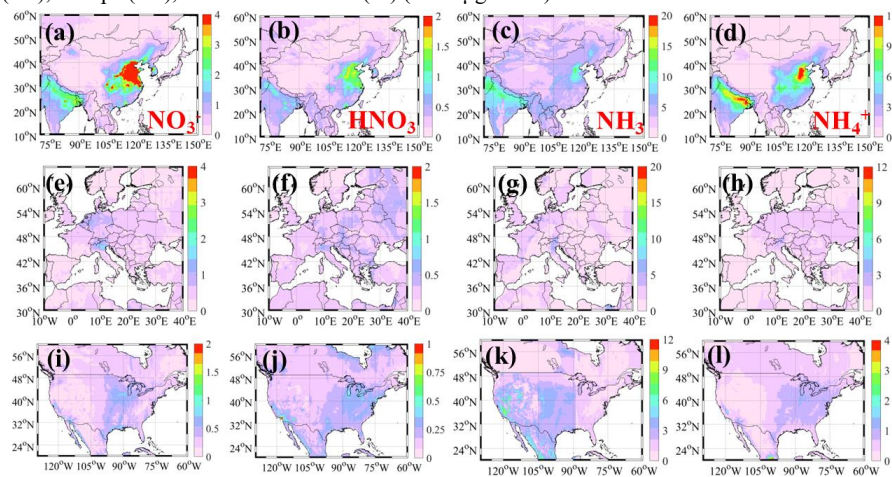
391 **Figure 2** The predictive performances of four reactive nitrogen components including NO_3^- (a),
392 HNO_3 (b), NH_3 (c), and NH_4^+ (d). The model was constructed with 90% original data and the
393 remained data was applied to validate the model. The black solid line denotes the best-fitting curve
394 for all of the points, while the black dashed line represents the diagonal, which means the same
395 observed and simulated values. The color scale denotes the sample size.



396



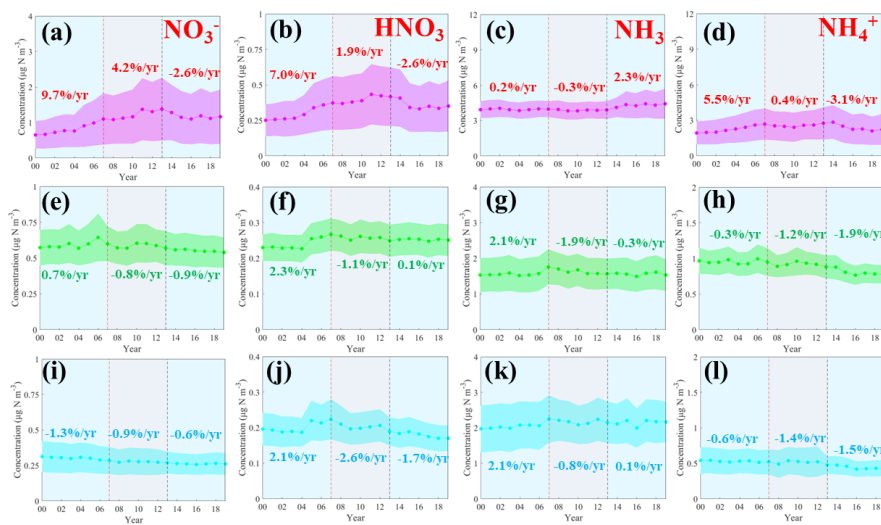
397 **Figure 3** The spatiotemporal variations of NO_3^- , HNO_3 , NH_3 , and NH_4^+ concentrations in East Asia
398 (a-d), Europe (e-h), and North America (i-l) (Unit: $\mu\text{g N m}^{-3}$).



399



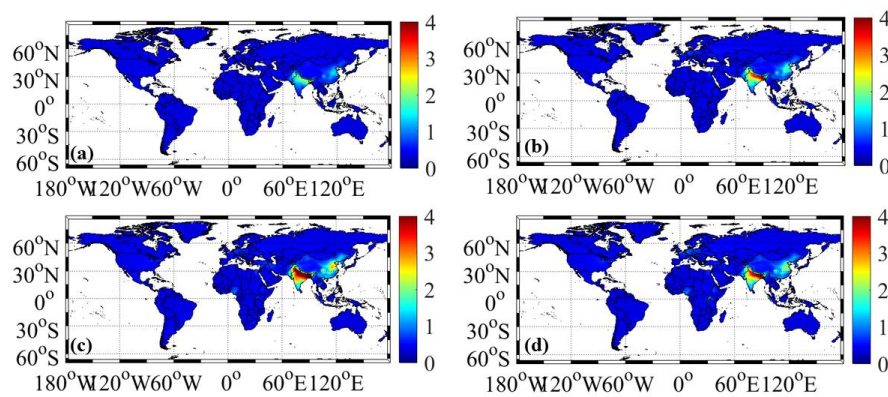
400 **Figure 4** The long-term variations of NO_3^- , HNO_3 , NH_3 , and NH_4^+ concentrations in China (pink),
 401 Europe (green), and the United States (cyan) (Unit: $\mu\text{g N m}^{-3}$).



402



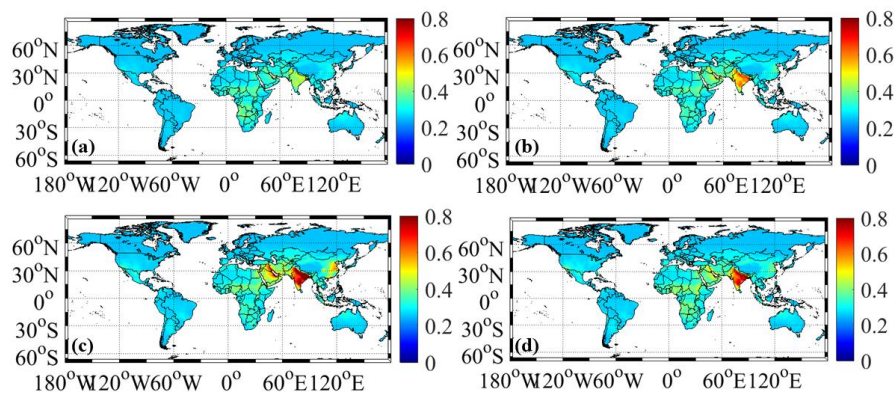
403 **Figure 5** Spatial variations of projected global ambient concentrations of reactive nitrogen
404 components under different climate change scenarios (Unit: $\mu\text{g N m}^{-3}$). Panels (a-d) represent the
405 annual mean concentrations of ambient NO_3^- under SSP1-2.6, SSP2-4.5, SSP3-7.0, and SSP5-8.5
406 during 2021-2100, respectively.



407
408



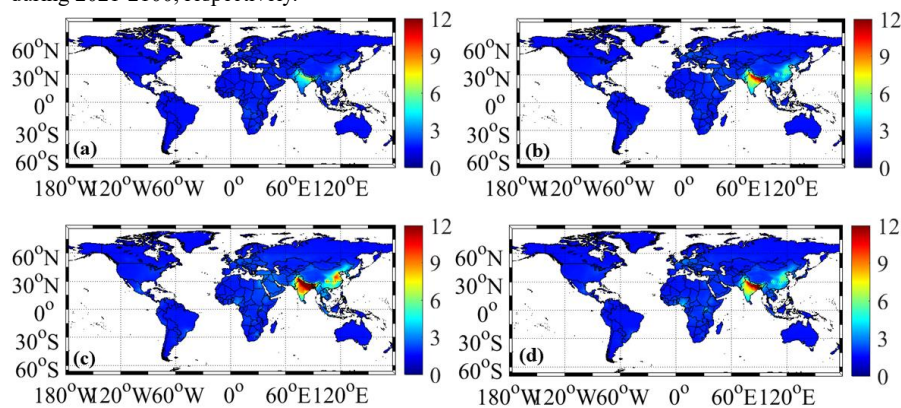
409 **Figure 6** Spatial variations of projected global ambient concentrations of reactive nitrogen
410 components under different climate change scenarios (Unit: $\mu\text{g N m}^{-3}$). Panels (a-d) represent the
411 annual mean concentrations of ambient HNO_3 under SSP1-2.6, SSP2-4.5, SSP3-7.0, and SSP5-8.5
412 during 2021-2100, respectively.



413
414



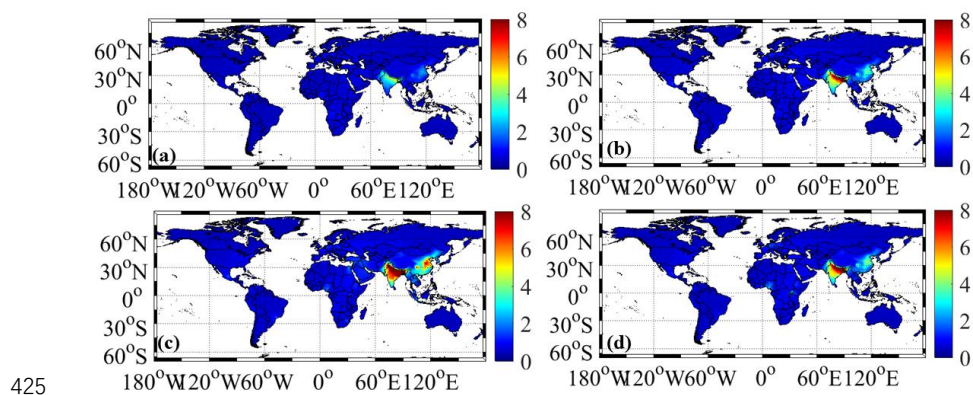
415 **Figure 7** Spatial variations of projected global ambient concentrations of reactive nitrogen
416 components under different climate change scenarios (Unit: $\mu\text{g N m}^{-3}$). Panels (a-d) represent the
417 annual mean concentrations of ambient NH_3 under SSP1-2.6, SSP2-4.5, SSP3-7.0, and SSP5-8.5
418 during 2021-2100, respectively.



419
420



421 **Figure 8** Spatial variations of projected global ambient concentrations of reactive nitrogen
422 components under different climate change scenarios (Unit: $\mu\text{g N m}^{-3}$). Panels (a-d) represent the
423 annual mean concentrations of ambient NH_4^+ under SSP1-2.6, SSP2-4.5, SSP3-7.0, and SSP5-8.5
424 during 2021-2100, respectively.





426 **References**

- 427 Altieri, K.E., Fawcett, S.E., Hastings, M.G. (2021) Reactive nitrogen cycling in the atmosphere and
428 ocean. *Annual Review of Earth and Planetary Sciences* 49, 523-550.
- 429 Amante, C., Eakins, B.W. (2009) ETOPO1 arc-minute global relief model: procedures, data sources and
430 analysis.
- 431 Bouwman, A., Van Vuuren, D., Derwent, R., Posch, M. (2002) A global analysis of acidification and
432 eutrophication of terrestrial ecosystems. *Water, Air, and Soil Pollution* 141, 349-382.
- 433 Chen, H., Li, D., Gurmesa, G.A., Yu, G., Li, L., Zhang, W., Fang, H., Mo, J. (2015) Effects of nitrogen
434 deposition on carbon cycle in terrestrial ecosystems of China: A meta-analysis. *Environmental pollution*
435 206, 352-360.
- 436 Chen, W., Lu, X., Yuan, D., Chen, Y., Li, Z., Huang, Y., Fung, T., Sun, H., Fung, J.C. (2023) Global PM_{2.5}
437 Prediction and Associated Mortality to 2100 under Different Climate Change Scenarios. *Environmental*
438 *science & technology* 57, 10039-10052.
- 439 Chen, X., Wang, Y.-h., Ye, C., Zhou, W., Cai, Z.-c., Yang, H., Han, X. (2018) Atmospheric nitrogen
440 deposition associated with the eutrophication of Taihu Lake. *Journal of Chemistry* 2018.
- 441 Chen, Y., Liu, A., Cheng, X. (2020) Quantifying economic impacts of climate change under nine future
442 emission scenarios within CMIP6. *Science of the Total Environment* 703, 134950.
- 443 Chen, Y., Shen, H., Russell, A.G. (2019) Current and future responses of aerosol pH and composition in
444 the US to declining SO₂ emissions and increasing NH₃ emissions. *Environmental science & technology*
445 53, 9646-9655.
- 446 Chen, Y., Zhang, L., Henze, D.K., Zhao, Y., Lu, X., Winiwarter, W., Guo, Y., Liu, X., Wen, Z., Pan, Y.
447 (2021) Interannual variation of reactive nitrogen emissions and their impacts on PM_{2.5} air pollution in
448 China during 2005–2015. *Environmental Research Letters* 16, 125004.
- 449 Cooper, M., Martin, R.V., Padmanabhan, A., Henze, D.K. (2017) Comparing mass balance and adjoint
450 methods for inverse modeling of nitrogen dioxide columns for global nitrogen oxide emissions. *Journal*
451 *of Geophysical Research: Atmospheres* 122, 4718-4734.
- 452 Cooper, M.J., Martin, R.V., Hammer, M.S., Levelt, P.F., Veefkind, P., Lamsal, L.N., Krotkov, N.A., Brook,
453 J.R., McLinden, C.A. (2022) Global fine-scale changes in ambient NO₂ during COVID-19 lockdowns.
454 *Nature* 601, 380-387.
- 455 Cui, L. (2023) Impact of COVID-19 restrictions on the concentration and source apportionment of
456 atmospheric ammonia (NH₃) across India. *Science of the Total Environment* 881, 163443.
- 457 Du, E., de Vries, W., Galloway, J.N., Hu, X., Fang, J. (2014) Changes in wet nitrogen deposition in the
458 United States between 1985 and 2012. *Environmental Research Letters* 9, 095004.
- 459 Ehrnsperger, L., Klemm, O. (2021) Source apportionment of urban ammonia and its contribution to
460 secondary particle formation in a Mid-size European City. *Aerosol and Air Quality Research* 21, 200404.
- 461 Feng, X., Lin, H., Fu, T.-M., Sulprizio, M.P., Zhuang, J., Jacob, D.J., Tian, H., Ma, Y., Zhang, L., Wang,
462 X. (2021) WRF-GC (v2. 0): online two-way coupling of WRF (v3. 9.1. 1) and GEOS-Chem (v12. 7.2)
463 for modeling regional atmospheric chemistry–meteorology interactions. *Geoscientific Model*
464 *Development* 14, 3741-3768.
- 465 Geddes, J.A., Martin, R.V. (2017a) Global deposition of total reactive nitrogen oxides from 1996 to 2014
466 constrained with satellite observations of NO₂ columns. *Atmos. Chem. Phys.* 17, 10071-10091.
- 467 He, Y., Pan, Y., Gu, M., Sun, Q., Zhang, Q., Zhang, R., Wang, Y. (2021) Changes of ammonia
468 concentrations in wintertime on the North China Plain from 2018 to 2020. *Atmospheric Research* 253,
469 105490.



- 470 He, Z., Liu, P., Zhao, X., He, X., Liu, J., Mu, Y. (2022) Responses of surface O₃ and PM_{2.5} trends to
471 changes of anthropogenic emissions in summer over Beijing during 2014–2019: A study based on
472 multiple linear regression and WRF-Chem. *Science of the Total Environment* 807, 150792.
- 473 Hoesly, R.M., Smith, S.J., Feng, L., Klimont, Z., Janssens-Maenhout, G., Pitkanen, T., Seibert, J.J., Vu,
474 L., Andres, R.J., Bolt, R.M. (2018) Historical (1750–2014) anthropogenic emissions of reactive gases
475 and aerosols from the Community Emissions Data System (CEDS). *Geoscientific Model Development*
476 11, 369–408.
- 477 Huang, L., An, J., Koo, B., Yarwood, G., Yan, R., Wang, Y., Huang, C., Li, L. (2019) Sulfate formation
478 during heavy winter haze events and the potential contribution from heterogeneous SO₂+NO₂ reactions
479 in the Yangtze River Delta region, China. *Atmospheric Chemistry and Physics* 19, 14311–14328.
- 480 Huang, T., Chen, J., Zhao, W., Cheng, J., Cheng, S. (2016) Seasonal variations and correlation analysis
481 of water-soluble inorganic ions in PM_{2.5} in Wuhan, 2013. *Atmosphere* 7, 49.
- 482 Huang, X., Liu, Z., Liu, J., Hu, B., Wen, T., Tang, G., Zhang, J., Wu, F., Ji, D., Wang, L. (2017) Chemical
483 characterization and source identification of PM_{2.5} at multiple sites in the Beijing–Tianjin–Hebei region,
484 China. *Atmospheric Chemistry and Physics* 17, 12941–12962.
- 485 Huneus, N., Granier, C., Dawidowski, L., van Der Gon, H.D., Alonso, M., Castesana, P., Diaz, M., Frost,
486 G.J., Gallardo, L., Gomez, D., (2017) Anthropogenic emissions in South America for air quality and
487 climate modelling, 2017 International Emission Inventory Conference “Applying Science and
488 Streamlining Processes to Improve Inventories”.
- 489 Kang, Y., Liu, M., Song, Y., Huang, X., Yao, H., Cai, X., Zhang, H., Kang, L., Liu, X., Yan, X. (2016)
490 High-resolution ammonia emissions inventories in China from 1980 to 2012. *Atmospheric Chemistry
491 and Physics* 16, 2043–2058.
- 492 Karra, K., Kontgis, C., Statman-Weil, Z., Mazzariello, J.C., Mathis, M., Brumby, S.P., (2021) Global
493 land use/land cover with Sentinel 2 and deep learning, 2021 IEEE international geoscience and remote
494 sensing symposium IGARSS. IEEE, pp. 4704–4707.
- 495 Kim, H.C., Lee, P., Judd, L., Pan, L., Lefer, B. (2016) OMI NO₂ column densities over North American
496 urban cities: the effect of satellite footprint resolution. *Geoscientific Model Development* 9, 1111–1123.
- 497 Li, H., Yang, Y., Wang, H., Wang, P., Yue, X., Liao, H. (2022) Projected aerosol changes driven by
498 emissions and climate change using a machine learning method. *Environmental science & technology*
499 56, 3884–3893.
- 500 Li, H., Zhang, Q., Zhang, Q., Chen, C., Wang, L., Wei, Z., Zhou, S., Parworth, C., Zheng, B., Canonaco,
501 F. (2017) Wintertime aerosol chemistry and haze evolution in an extremely polluted city of the North
502 China Plain: significant contribution from coal and biomass combustion. *Atmospheric Chemistry and
503 Physics* 17, 4751–4768.
- 504 Li, R., Cui, L., Fu, H., Zhao, Y., Zhou, W., Chen, J. (2020) Satellite-Based Estimates of Wet Ammonium
505 (NH₄-N) Deposition Fluxes Across China during 2011–2016 Using a Space–Time Ensemble Model.
506 *Environmental science & technology* 54, 13419–13428.
- 507 Li, R., Cui, L., Zhao, Y., Zhang, Z., Sun, T., Li, J., Zhou, W., Meng, Y., Huang, K., Fu, H. (2019a) Wet
508 deposition of inorganic ions in 320 cities across China: spatio-temporal variation, source apportionment,
509 and dominant factors. *Atmospheric Chemistry and Physics* 19, 11043–11070.
- 510 Li, R., Gao, Y., Xu, J., Cui, L., Wang, G. (2023) Impact of Clean Air Policy on Criteria Air Pollutants
511 and Health Risks Across China During 2013–2021. *Journal of Geophysical Research: Atmospheres* 128,
512 e2023JD038939.
- 513 Li, R., Wang, Z., Cui, L., Fu, H., Zhang, L., Kong, L., Chen, W., Chen, J. (2019b) Air pollution



514 characteristics in China during 2015–2016: Spatiotemporal variations and key meteorological factors.
515 *Science of the Total Environment* 648, 902-915.

516 Li, Y., Schichtel, B.A., Walker, J.T., Schwede, D.B., Chen, X., Lehmann, C.M., Puchalski, M.A., Gay,
517 D.A., Collett Jr, J.L. (2016) Increasing importance of deposition of reduced nitrogen in the United States.
518 *Proceedings of the National Academy of Sciences* 113, 5874-5879.

519 Lin, W., Xu, X., Ge, B., Liu, X. (2011) Gaseous pollutants in Beijing urban area during the heating period
520 2007–2008: variability, sources, meteorological, and chemical impacts. *Atmospheric Chemistry and*
521 *Physics* 11, 8157-8170.

522 Liu, H., Gong, P., Wang, J., Clinton, N., Bai, Y., Liang, S. (2020a) Annual dynamics of global land cover
523 and its long-term changes from 1982 to 2015. *Earth System Science Data* 12, 1217-1243.

524 Liu, H., Jacob, D.J., Bey, I., Yantosca, R.M. (2001) Constraints from ²¹⁰Pb and ⁷Be on wet deposition
525 and transport in a global three-dimensional chemical tracer model driven by assimilated meteorological
526 fields. *Journal of Geophysical Research: Atmospheres* 106, 12109-12128.

527 Liu, L., Yang, Y., Xi, R., Zhang, X., Xu, W., Liu, X., Li, Y., Liu, P., Wang, Z. (2021) Global Wet-Reduced
528 Nitrogen Deposition Derived From Combining Satellite Measurements With Output From a Chemistry
529 Transport Model. *Journal of Geophysical Research: Atmospheres* 126, e2020JD033977.

530 Liu, L., Zhang, X., Wong, A.Y., Xu, W., Liu, X., Li, Y., Mi, H., Lu, X., Zhao, L., Wang, Z. (2019)
531 Estimating global surface ammonia concentrations inferred from satellite retrievals. *Atmospheric*
532 *Chemistry and Physics* 19, 12051-12066.

533 Liu, L., Zhang, X., Xu, W., Liu, X., Lu, X., Wei, J., Li, Y., Yang, Y., Wang, Z., Wong, A.Y. (2020b)
534 Reviewing global estimates of surface reactive nitrogen concentration and deposition using satellite
535 retrievals. *Atmospheric Chemistry and Physics* 20, 8641-8658.

536 Liu, Y., Zhou, Y., Lu, J. (2020c) Exploring the relationship between air pollution and meteorological
537 conditions in China under environmental governance. *Scientific reports* 10, 14518.

538 Luo, Z., Zhang, Y., Chen, W., Van Damme, M., Coheur, P.-F., Clarisse, L. (2022) Estimating global
539 ammonia (NH₃) emissions based on IASI observations from 2008 to 2018. *Atmospheric Chemistry and*
540 *Physics* 22, 10375-10388.

541 Ma, R., Yu, K., Xiao, S., Liu, S., Ciais, P., Zou, J. (2022) Data-driven estimates of fertilizer-induced soil
542 NH₃, NO and N₂O emissions from croplands in China and their climate change impacts. *Global Change*
543 *Biology* 28, 1008-1022.

544 McDuffie, E.E., Smith, S.J., O'Rourke, P., Tibrewal, K., Venkataraman, C., Marais, E.A., Zheng, B.,
545 Crippa, M., Brauer, M., Martin, R.V. (2020) A global anthropogenic emission inventory of atmospheric
546 pollutants from sector-and fuel-specific sources (1970–2017): an application of the Community
547 Emissions Data System (CEDS). *Earth System Science Data* 12, 3413-3442.

548 Nazarenko, L.S., Tausnev, N., Russell, G.L., Rind, D., Miller, R.L., Schmidt, G.A., Bauer, S.E., Kelley,
549 M., Ruedy, R., Ackerman, A.S. (2022) Future climate change under SSP emission scenarios with GISS-
550 E2. 1. *Journal of Advances in Modeling Earth Systems* 14, e2021MS002871.

551 Pan, Y., Tian, S., Zhao, Y., Zhang, L., Zhu, X., Gao, J., Huang, W., Zhou, Y., Song, Y., Zhang, Q. (2018)
552 Identifying ammonia hotspots in China using a national observation network. *Environmental science &*
553 *technology* 52, 3926-3934.

554 Paulot, F., Jacob, D.J., Pinder, R., Bash, J., Travis, K., Henze, D. (2014) Ammonia emissions in the
555 United States, European Union, and China derived by high-resolution inversion of ammonium wet
556 deposition data: Interpretation with a new agricultural emissions inventory (MASAGE_NH₃). *Journal*
557 *of Geophysical Research: Atmospheres* 119, 4343-4364.



- 558 Potapov, P., Hansen, M.C., Pickens, A., Hernandez-Serna, A., Tyukavina, A., Turbanova, S., Zalles, V.,
559 Li, X., Khan, A., Stolle, F. (2022) The global 2000-2020 land cover and land use change dataset derived
560 from the Landsat archive: first results. *Frontiers in Remote Sensing* 3, 856903.
- 561 Qi, L., Zheng, H., Ding, D., Wang, S. (2023) Responses of sulfate and nitrate to anthropogenic emission
562 changes in eastern China-in perspective of long-term variations. *Science of the Total Environment* 855,
563 158875.
- 564 Qu, Z., Henze, D.K., Cooper, O.R., Neu, J.L. (2020) Impacts of global NO_x inversions on NO₂ and
565 ozone simulations. *Atmospheric Chemistry and Physics* 20, 13109-13130.
- 566 Shi, X., Zhao, C., Jiang, J.H., Wang, C., Yang, X., Yung, Y.L. (2018) Spatial representativeness of PM_{2.5}
567 concentrations obtained using observations from network stations. *Journal of Geophysical Research:*
568 *Atmospheres* 123, 3145-3158.
- 569 Van Damme, M., Whitburn, S., Clarisse, L., Clerbaux, C., Hurtmans, D., Coheur, P.-F. (2017) Version 2
570 of the IASI NH₃ neural network retrieval algorithm: near-real-time and reanalysed datasets.
571 *Atmospheric Measurement Techniques* 10, 4905-4914.
- 572 Von Schneidemesser, E., Monks, P.S., Allan, J.D., Bruhwiler, L., Forster, P., Fowler, D., Lauer, A.,
573 Morgan, W.T., Paasonen, P., Righi, M. (2015) Chemistry and the linkages between air quality and climate
574 change. *Chemical reviews* 115, 3856-3897.
- 575 Wang, M., Xiao, M., Bertozzi, B., Marie, G., Rörup, B., Schulze, B., Bardakov, R., He, X.-C., Shen, J.,
576 Scholz, W. (2022) Synergistic HNO₃-H₂SO₄-NH₃ upper tropospheric particle formation. *Nature* 605,
577 483-489.
- 578 Wang, T., Song, Y., Xu, Z., Liu, M., Xu, T., Liao, W., Yin, L., Cai, X., Kang, L., Zhang, H., Zhu, T. (2020)
579 Why is the Indo-Gangetic Plain the region with the largest NH₃ column in the globe during pre-monsoon
580 and monsoon seasons? *Atmos. Chem. Phys.* 20, 8727-8736.
- 581 Wang, Y., Li, W., Gao, W., Liu, Z., Tian, S., Shen, R., Ji, D., Wang, S., Wang, L., Tang, G. (2019) Trends
582 in particulate matter and its chemical compositions in China from 2013–2017. *Science China Earth*
583 *Sciences* 62, 1857-1871.
- 584 Warner, J., Dickerson, R., Wei, Z., Strow, L.L., Wang, Y., Liang, Q. (2017) Increased atmospheric
585 ammonia over the world's major agricultural areas detected from space. *Geophysical Research Letters*
586 44, 2875-2884.
- 587 Wen, L., Xue, L., Wang, X., Xu, C., Chen, T., Yang, L., Wang, T., Zhang, Q., Wang, W. (2018)
588 Summertime fine particulate nitrate pollution in the North China Plain: increasing trends, formation
589 mechanisms and implications for control policy. *Atmospheric Chemistry and Physics* 18, 11261-11275.
- 590 Wesely, M. (2007) Parameterization of surface resistances to gaseous dry deposition in regional-scale
591 numerical models. *Atmospheric Environment* 41, 52-63.
- 592 Whitburn, S., Van Damme, M., Clarisse, L., Bauduin, S., Heald, C., Hadji-Lazaro, J., Hurtmans, D.,
593 Zondlo, M.A., Clerbaux, C., Coheur, P.F. (2016a) A flexible and robust neural network IASI-NH₃
594 retrieval algorithm. *Journal of Geophysical Research: Atmospheres* 121, 6581-6599.
- 595 Whitburn, S., Van Damme, M., Clarisse, L., Turquety, S., Clerbaux, C., Coheur, P.F. (2016b) Doubling
596 of annual ammonia emissions from the peat fires in Indonesia during the 2015 El Niño. *Geophysical*
597 *Research Letters* 43, 11,007-011,014.
- 598 Xu, L., Chen, X., Chen, J., Zhang, F., He, C., Zhao, J., Yin, L. (2012) Seasonal variations and chemical
599 compositions of PM_{2.5} aerosol in the urban area of Fuzhou, China. *Atmospheric Research* 104, 264-
600 272.
- 601 Xu, W., Zhang, L., Liu, X. (2019) A database of atmospheric nitrogen concentration and deposition from



602 the nationwide monitoring network in China. *Scientific data* 6, 1-6.
603 Zaehle, S. (2013) Terrestrial nitrogen–carbon cycle interactions at the global scale. *Philosophical*
604 *Transactions of the Royal Society B: Biological Sciences* 368, 20130125.
605 Zhang, L., Guo, X., Zhao, T., Gong, S., Xu, X., Li, Y., Luo, L., Gui, K., Wang, H., Zheng, Y. (2019) A
606 modelling study of the terrain effects on haze pollution in the Sichuan Basin. *Atmospheric Environment*
607 196, 77-85.
608 Zhang, X., Ward, B.B., Sigman, D.M. (2020) Global nitrogen cycle: critical enzymes, organisms, and
609 processes for nitrogen budgets and dynamics. *Chemical reviews* 120, 5308-5351.
610 Zhang, X., Wu, Y., Liu, X., Reis, S., Jin, J., Dragosits, U., Van Damme, M., Clarisse, L., Whitburn, S.,
611 Coheur, P.-F. (2017) Ammonia emissions may be substantially underestimated in China. *Environmental*
612 *science & technology* 51, 12089-12096.
613 Zhang, Y., Mathur, R., Bash, J.O., Hogrefe, C., Xing, J., Roselle, S.J. (2018) Long-term trends in total
614 inorganic nitrogen and sulfur deposition in the US from 1990 to 2010. *Atmospheric Chemistry and*
615 *Physics* 18, 9091-9106.
616
617